RSC Applied Interfaces

ROYAL SOCIETY OF CHEMISTRY

PAPER

View Article Online
View Journal | View Issue

Cite this: *RSC Appl. Interfaces*, 2025, **2**, 1784

N-type semiconducting polymers with an improved isotropic mobility–stretchability stability by using structural isomers as conjugation break spacers

Ming-Han Chen,[a] Yu-Chun Huang,[a] Fu-En Szu,[b] Jung-Yao Chen,[c] Man-kit Leung[bd] and Yan-Cheng Lin *[ad]

The structural isomeric effect on the conjugation-break spacers (CBSs) design in stretchable conjugated polymers hasn't been investigated. In addition, achieving isotropic mobility–stretchability performance is challenging, as crack formation and polymer chain alignment can make the mobility anisotropic. In this study, three alicyclic CBSs were incorporated into the backbone of naphthalenediimide (NDI)-based n-type semiconducting polymers to enhance their mechanical and electronic performance. Of the three CBSs, 2,5-tricyclodecanedimethanol (TCD–CBS) and an isomeric mixture of tricyclodecanedimethanol (*r*TCDs–CBS) feature tricyclic structures derived from dicyclopentadiene, whereas *trans*-1,4-cyclohexanediol (*t*CH–CBS) incorporates a monocyclic structure. The experimental results demonstrate that the structural configuration of the CBS units has a significant influence on polymer aggregation, crystallinity, chain alignment, and mechanical stability. **TCD**, with its rigid tricyclic structure of TCD–CBS that promotes predominant face-on stacking, delivers high initial mobility but lacks mechanical durability under strain. In contrast, ***t*CH** features a flexible monocyclic structure of *t*CH–CBS that favors edge-on stacking, enables isotropic transport, but suffers from low mobility and poor structural stability due to its high chain conformability under deformation. However, unlike **TCD** and ***t*CH**, ***r*TCDs** comprising *r*TCDs–CBS offers balanced performance by introducing moderate structural disorder that supports a bimodal molecular orientation. This configuration increases free volume and creates additional charge carrier pathways, allowing the polymer to maintain ductility and stable charge transport under strain. After 1000 cycles at 40% strain, ***r*TCDs** retained 77% of their mobility in the parallel direction and 104% in the perpendicular direction, relative to single-cycle performance. These results highlight the potential of isomeric design in CBS units to achieve both mechanical flexibility and isotropic electronic performance in stretchable semiconducting polymers for wearable and deformable electronics.

Received 15th July 2025,
Accepted 5th September 2025

DOI: 10.1039/d5lf00196j

rsc.li/RSCApplInter

1. Introduction

The demand for flexibility, portability, and seamless integration with the human body is driving the evolution of modern electronics.[1] As technologies such as wearable sensors, bioelectronic interfaces, and soft robotics continue to advance, conventional rigid electronics like silicon are proving insufficient. Conjugated polymers, with their tunable electronic properties and intrinsic softness, have emerged as a key enabler for next-generation flexible devices. These materials support a broad range of flexible and stretchable electronic applications, including organic field-effect transistors (OFETs),[1–3] organic electrochemical transistors (OECTs),[4,5] organic photovoltaics (OPVs),[6,7] and organic light-emitting diodes (OLEDs).[8–10] Among these, recent advances in OFET development are particularly notable. For example, the incorporation of non-planar p–π conjugation units into a DPP-based terpolymer backbone maintains intrachain charge transport while inducing backbone twisting, achieving a mobility of ~0.21 $cm^2 V^{-1} s^{-1}$ at 150% strain and retaining performance after 1000 stretch–release cycles at 50% strain.[11] A side-chain crosslinking strategy using benzophenone-derived small molecules with flexible oligomeric linkers has been developed to restrict chain slippage through covalent bonding and dissipate strain energy through rotational

[a] *Department of Chemical Engineering, National Cheng Kung University, Tainan 70101, Taiwan. E-mail: ycl@gs.ncku.edu.tw*
[b] *Department of Chemistry, National Taiwan University, Taipei 10617, Taiwan*
[c] *Department of Photonics, National Cheng Kung University, Tainan City 70101, Taiwan*
[d] *Advanced Research Center for Green Materials Science and Technology, National Taiwan University, Taipei 10617, Taiwan*

freedom.[12] However, despite extensive studies, research has primarily focused on optimizing p-type mobility, with limited progress in n-type semiconductors due to the scarcity of stable electron-deficient acceptors and their high sensitivity to oxidative degradation.

To overcome the inherent challenges of n-type polymer semiconductors, various design strategies have been explored, including elastomer blending, side-chain engineering, and main-chain engineering.[13,14] Elastomer blending physically combines stretchable elastomers with conjugated polymers to enhance chain mobility and suppress large crystalline domains.[15–18] However, poor thermal stability, along with processing challenges such as optimizing the blending ratio, has hindered its broader applications.[13] Meanwhile, side-chain engineering has been shown to weaken intermolecular π–π interactions and promote localized aggregation in conjugated polymers.[19,20] Yet, its influence on intrinsic properties such as charge mobility and mechanical strength is limited, as it primarily tunes morphology rather than the backbone structure.[21] In contrast, main-chain engineering has received the most attention for its ability to directly modify the intrinsic properties directly, enabling precise tuning of intrinsic properties.[22] Strategies such as conjugation break spacers (CBSs),[23–25] block copolymers,[26,27] hydrogen bonding,[28,29] and atom-knotting[30] have been extensively investigated to enhance both mechanical flexibility and charge transport. The implementation of block copolymers has been reported to achieve phase segregation and enhanced mechanical properties, facilitating charge transport through ordered conjugated domains while absorbing mechanical stress under strain. Hydrogen bonding also enhances performance by acting as a dynamic, reversible non-covalent cross-link that dissipates strain energy and allows flexibility. However, block copolymers with precise molecular characteristics are synthetically demanding, while hydrogen bonding may introduce torsional strain or steric hindrance that disrupts π–conjugation and reduces charge mobility.[13] Within these design strategies, the incorporation of CBSs with flexible non-conjugated linkers provides a promising approach for maintaining both electrical and mechanical performance.[18]

Recent advances in intrinsically stretchable semiconducting polymers have been driven by the integration of CBSs, which feature structural designs ranging from flexible chains to asymmetric geometries. The introduction of long, flexible alkyl CBSs increases chain mobility and reduces modulus, thereby enhancing ductility and crack-onset strain with minimal impact on charge transport.[31] Meanwhile, sterically asymmetric CBSs have been shown to alter backbone geometry by disrupting central symmetry, which reduces crystallinity and tensile modulus while preserving π–π stacking.[32] Building on success in p-type systems, recent research has extended these design strategies to n-type polymers. For instance, three biobased dianhydrohexoses epimers of isosorbide (ISB), isomannide (IMN), and isoidide (IID) were incorporated into naphthalenediimide (NDI)-based polymers *via* a Stille coupling reaction. Among them, ISB, characterized by an *endo*-/*exo*-configurations and rigid bicyclic structure, promotes chain realignment and stress dissipation, resulting in lower crack density and improved charge transport under strain.[25] While CBS-based designs have shown substantial promise for enhancing stretchability, the role of structural isomerism remains underexplored. This study provides an in-depth investigation of the impact of CBS structural complexity on morphology and the mobility–stretchability relationship in n-type semiconducting polymers.

In recent years, the role of chemistry has evolved from resource-to-waste conversion to resource recovery and recycling, aligning more closely with the principles of environmental sustainability.[33] Dicyclopentadiene (DCPD), a byproduct of C5 streams in oil refineries, has gained attention due to its unique combination of high thermal stability, low polarity, and bulky, rigid structure. Its tricyclic fused-ring architecture has enabled applications in surface coating systems, adhesives, and epoxy resin hardeners.[34,35] Moreover, DCPD-derived intermediates have shown promise as monomeric precursors for polyesters, polyurethanes, and polyamides.[36,37] Nonetheless, the incorporation of DCPD-derived monomers into semiconducting polymer systems has remained relatively underexplored. In this study, we introduce structural and regio-random tricyclodecane-based CBS (*r*TCDs–CBS), as a novel CBS for constructing semiconducting polymer backbones. We further examined the effects of structural complexity in the tricyclic structure by incorporating a structural and regio-selective 2,5-tricyclodecane-based CBS (TCD–CBS) and *trans*-1,4-cyclohexane-based CBS (*t*CH–CBS) into the polymer backbone, comparing them to a reference **PNDI2T** polymer without any CBS. Their mobility–stretchability performance was evaluated through FET measurements, alongside detailed characterization of their morphological, optical, and mechanical properties. Statistical analysis revealed that increasing structural complexity helps preserve mobility isotropy and enhance durability under cyclic strain. The isomeric mixture in ***r*TCDs** polymer yielded the most balanced performance, while **TCD** and ***t*CH** exhibited lower mechanical resilience and reduced charge transport after repeated cycles. These results suggest that the structural complexity and rigidity of ***r*TCDs** contribute to an optimized morphology that accommodates mechanical deformation while maintaining efficient and isotropic charge carrier pathways.

2. Experimental section

2.1 Materials

N,*N*′-Dicyclohexylcarbodiimide (DCC, ≥99%) was purchased from Thermo Scientific Chemicals. 4-Dimethylaminopyridine (DMAP, ≥99%), (1*S*,4*S*)-cyclohexane-1,4-diol (*t*CH–diol, >97%), and octahydro-4,7-methano-1*H*-indenedimethanol (*r*TCDs–diol, mixture of isomers, >90 wt% of three isomers in Scheme 1) were purchased from Tokyo Chemical Industry. Octahydro-4,7-methano-1*H*-indene-2,5-dimethanol (TCD–diol) was synthesized according to a reported method.[34–36]

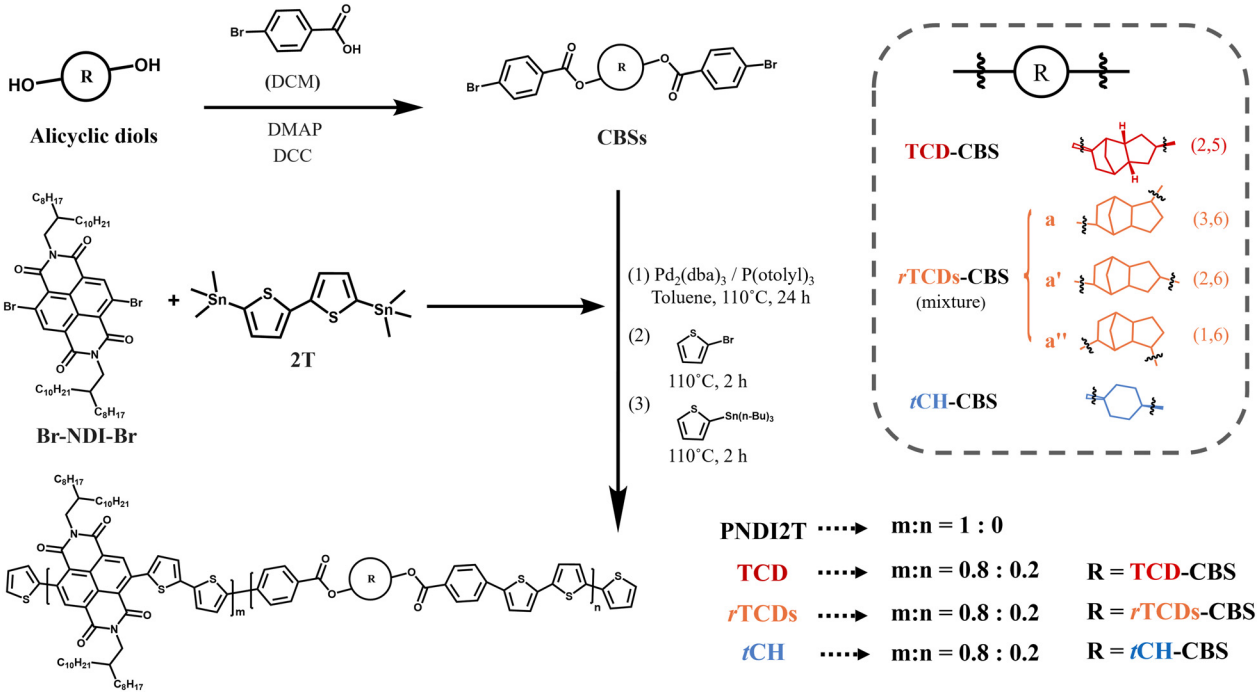

Scheme 1 Chemical structures and synthetic route of the N-type conjugated polymers incorporating alicyclic units as conjugation break spacers (CBSs) and their copolymerization compositions. Note that the TCD–CBS is in an *endo* configuration with pure 2,5 structure selectivity, and the *r*TCDs–CBS are in mixed *endo*/*exo* configurations with the 3,6-, 2,6-, and 1,6-isomers accounting for 90 wt% of the mixture from the commercial source.

4,9-Dibromo-2,7-bis(2-octyldodecyl)benzo-[*lmn*][3,8]-phenanthroline-1,3,6,8(2*H*,7*H*)-tetraone (NDA–Br_2) was synthesized according to previously reported methods.[38] All other reagents and solvents were purchased from Thermo Scientific Chemicals, Sigma-Aldrich, Tokyo Chemical Industry, ACROS, and Alfa Aesar, and used as received without further purification unless otherwise specified.

2.2 Synthesis of (octahydro-1*H*-4,7-methanoindenediyl)bis(methylene)bis(4-bromobenzoate) (*r*TCDs–CBS)

*r*TCDs–diol (0.589 g, 3.001 mmol), 4-bromobenzoic acid (1.821 g, 9.059 mmol), DCM (25 ml), and DMAP (0.07 g, 0.573 mmol) were placed in a 100 mL round-bottom flask. To this solution, DCC (1.36 g, 6.60 mmol) was then added portion-wise while stirring in the ice bath. The reaction mixture was subsequently stirred at room temperature and refluxed for 24 h. After the reaction, the mixture was extracted with dichloromethane and washed with water and brine. The obtained organic phase was dried over magnesium sulfate, filtered, and rotary evaporated. The crude product was then purified by silica gel chromatography using DCM as an eluent to afford an orange solid (1.014 g, 60.1%). ^{1}H NMR (700 MHz, $CDCl_3$, δ ppm, 25 °C, Fig. 1b): 7.88 (m, Ar–**H**, 4H), 7.58 (m, Ar–**H**, 4H), 4.66 (m, CO–C**H**$_2$–Bc, 2H), 4.16 (m, CO–C**H**$_2$–Cy, 2H), 2.57–0.87(m, Tc–**H**, 14H) ^{13}C NMR (500 MHz, $CDCl_3$, δ ppm, 25 °C, Fig. S1): 24.49, 25.22, 27.77, 28.30, 32.87, 34.35, 38.24, 39.45, 40.34, 41.55, 42.98, 43.12, 44.60, 45.14, 49.15, 49.96, 123.53, 127.99, 130.65, 131.06, 131.64, 166.00. Anal. calcd. for $C_{26}H_{26}Br_2O_4$ (%): C, 55.54; H, 4.66. Found (%): C, 55.90; H, 4.50.

2.3 Synthesis of (octahydro-1*H*-4,7-methanoindene-2,5-diyl)bis(methylene)bis(4-bromobenzoate) (TCD–CBS)

TCD–diol (0.200 g, 1.02 mmol), 4-bromobenzoic acid (0.604 g, 3.00 mmol), DCM (25 ml), DCC (0.490 g, 2.37 mmol), and DMAP (0.025 g, 0.205 mmol) were applied. All other reaction conditions and purification procedures followed those described in the previous section. After gel permeation chromatography, a white solid was obtained in a 40.5% (0.227 g) yield. ^{1}H NMR (700 MHz, $CDCl_3$, δ ppm, 25 °C, Fig. 1a): 7.88 (m, Ar–**H**, 4H), 7.58 (m, Ar–**H**, 4H), 4.66 (m, CO–C**H**$_2$–Bc, 2H), 4.16 (m, CO–C**H**$_2$–Cy, 2H), 2.57–0.87(m, Tc–**H**, 14H) ^{13}C NMR (500 MHz, $CDCl_3$, δ ppm, 25 °C, Fig. S2): 26.97, 28.57, 30.86, 40.23, 41.60, 43.43, 44.98, 45.59, 46.76, 68.12, 127.92, 129.34, 131.07, 131.70, 165.70. Anal. calcd. for $C_{26}H_{26}Br_2O_4$ (%): C, 55.54; H, 4.66. Found (%): C, 55.24; H, 4.46.

2.4 Synthesis of (1*S*,4*S*)-cyclohexane-1,4-diyl-bis(4-bromobenzoate) (*t*CH–CBS)

*t*CH–diol (0.119 g, 1.024 mmol), 4-bromobenzoic acid (0.604 g, 3.004 mmol), DCM (5 ml), DCC (0.428 g, 2.072 mmol), and DMAP (0.022 g, 0.180 mmol) were applied. All other reaction conditions and purification procedures followed those described in the previous section. After gel permeation

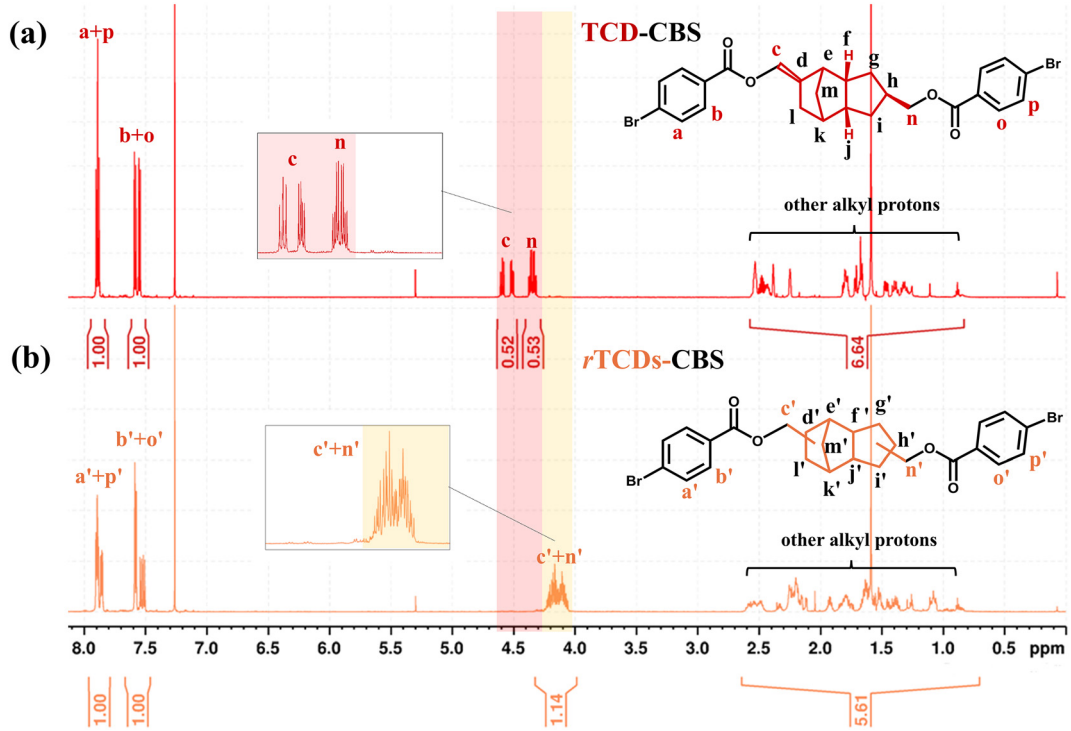

Fig. 1 ^{1}H NMR spectral differences highlighting the structural distinction between (a) the structurally and regio-selective TCD–CBS and (b) the structurally and regio-random *r*TCDs–CBS.

chromatography, a white solid was obtained in a 20.3% yield (0.100 g). ^{1}H NMR (700 MHz, $CDCl_3$, δ ppm, 25 °C, Fig. S3): 7.96 (d, Ar–**H**, 4H), 7.55 (d, Ar–**H**, 4H), 5.14 (m, C**H**–O–CO, 2H), 2.12 (m, CH–C**H$_2$**–CH_2, 4H), 1.86 (m, CH–CH_2–C**H$_2$**, 4H). ^{13}C NMR (500 MHz, $CDCl_3$, δ ppm, 25 °C, Fig. S4): 27.90, 71.64, 128.13, 129.42, 131.13, 131.71, 165.31. Anal. calcd. for $C_{20}H_{18}Br_2O_4$ (%): C, 49.82; H, 3.76. Found (%): C, 48.20; H, 3.77.

2.5 General procedure for Stille coupling polymerization

The synthetic procedures for the three polymers studied are shown in Scheme 1. For a typical synthesis of ***r*TCDs**, a two-neck 50 mL round-bottom flask was charged with 2T (174 mg, 0.354 mmol), Br–NDA–Br_2 (280 mg, 0.284 mmol), and *r*TCDs–CBS (40.3 mg, 0.072 mmol). After dissolving them in chlorobenzene (6 mL), N_2 was bubbled through the solution for 30 min. $Pd_2(dba)_3$ (37.7 mg, 0.041 mmol) and P(*o*-tolyl)$_3$ (110 mg, 0.362 mmol) were then added to the mixture, and the solution was stirred at 130 °C for 24 h. After the reaction, 2-bromothiophene (18 μL) and 2-(tributylstannyl)thiophene (56 μL) were added to serve as end-capping agents, and the solution was stirred at 130 °C for 2 hours for each end-cap reaction. After cooling to room temperature, the crude polymer was precipitated into methanol and filtered. The polymeric product was then purified by Soxhlet extraction using acetone and hexane and recovered with chloroform (24 h for each). The chloroform solution collected was condensed by evaporation under reduced pressure to afford ***r*TCDs** as a blue solid in 58.9% (260 mg) yield. The ^{1}H and ^{13}C NMR spectra are shown in Fig. S5 and S6 (SI).

TCD. 2T (174 mg, 0.354 mmol), Br–NDI–Br (293 mg, 0.297 mmol), and TCD–CBS (35.4 mg, 0.063 mmol), chlorobenzene (6 mL), $Pd_2(dba)_3$ (37.0 mg, 0.040 mmol), P(*o*-tolyl)$_3$ (112 mg, 0.367 mmol), 2-bromothiophene (18 μL), and 2-(tributylstannyl)thiophene (56 μL). Blue solid (315 mg, 68.1%). The ^{1}H and ^{13}C NMR spectra are shown in Fig. S7 and S8 (SI).

***t*CH.** 2T (182 mg, 0.370 mmol), Br–NDI–Br (292 mg, 0.297 mmol), and *t*CH–CBS (30.6 mg, 0.063 mmol), chlorobenzene (6 mL), $Pd_2(dba)_3$ (41.4 mg, 0.045 mmol), P(*o*-tolyl)$_3$ (120 mg, 0.396 mmol), 2-bromothiophene (18 μL), and 2-(tributylstannyl)thiophene (56 μL). Blue solid (311 mg, 69.6%). The ^{1}H and ^{13}C NMR spectra are shown in Fig. S9 and S10 (SI).

2.6 Characterization

^{1}H and ^{13}C nuclear magnetic resonance (NMR) spectra were recorded using a Bruker AVIIIHD 700 MHz spectrometer. All samples were dissolved in $CDCl_3$ before measurement. Elemental analysis was conducted using a UNICUBE analyzer (Elementar, Germany) to determine the elemental composition of the polymers. Gel permeation chromatography (GPC) was used to determine the number-average molecular weight (M_n), weight-average molecular weight (M_w), and polydispersity index ($Đ_M$). Measurements

were conducted using an LC-20AT pump, SIL-20A autosampler, CTO-20A column oven, and RID-20A detector, with THF containing 0.02–0.03% BHT as the mobile phase. Cyclic voltammetry was performed using a CHI 6273E workstation with a three-electrode setup, where the polymer-coated ITO served as the working electrode, platinum foil as the counter electrode, and a silver wire in $Ag/AgNO_3$ as the reference electrode. The electrolyte was 0.1 M tetrabutylammonium perchlorate in acetonitrile. The optical properties of polymer solutions and thin films were examined using a JASCO V-770 UV-vis/NIR spectrophotometer. Dichroic ratios of strained polymer films were determined on the same instrument by measuring polarized absorbance with incident light polarized parallel and perpendicular to the strain direction. Thermal properties of the polymers were characterized using PerkinElmer instruments. The melting temperature (T_m), enthalpy of fusion (ΔH_f), and entropy of fusion (ΔS_f) were measured with a DSC 6000 differential scanning calorimeter. The decomposition temperature ($T_d^{5\%}$) was determined using a TGA 4000 thermogravimetric analyzer under a nitrogen atmosphere. Dynamic mechanical analysis (DMA) was performed using an ARES G2 instrument to determine the glass transition temperature (T_g). Measurements were conducted at a frequency of 1 Hz, with a strain of 0.1%, a preload of 0.05 N, and a heating rate of 5 °C min^{-1}. Polymer film morphology and force mapping were examined using an AFM100plus atomic force microscope by Hitachi and a Microtech MX53-RF optical microscope. Grazing-incidence wide-angle X-ray scattering (GIWAXS) measurements were performed at beamline 23A1 of the Taiwan Light Source, NSRRC, using a monochromatic beam (λ = 1.24 Å) at a 0.2° incidence angle on silicon-supported films.

2.7 Device fabrications and measurements

The field-effect transistors (FETs) were fabricated using a bottom-gate/top-contact (BG/TC) configuration, with the polymer film serving as the active charge transport layer. A polymer solution (5 mg mL^{-1}) was spin-coated at 1500 rpm for 30 s onto an octadecyltrichlorosilane (ODTS)-modified silicon wafer with a 300 nm-thick thermally grown SiO_2 layer (areal capacitance = 10 nF cm^{-2}). The resulting films were thermally annealed at 220 °C for 30 min under vacuum. Subsequently, 40 nm-thick gold electrodes were thermally evaporated through a shadow mask to define the source and drain contacts, yielding a channel length (L) of 50 μm and width (W) of 1000 μm. All fabrication processes were conducted in a nitrogen-filled glove box to prevent exposure to ambient conditions. To evaluate mechanical durability and charge transport behavior under strain, a film-transfer technique was employed. The polymer film was stripped from the ODTS-treated substrate using a poly(dimethylsiloxane) (PDMS) slab prepared with a 20 : 1 (w/w) base-to-crosslinker ratio. After applying the desired strain to the PDMS-supported film, it was transferred onto a fresh Si/SiO_2 substrate with the same dielectric thickness. A second gold electrode array was then deposited through the same shadow mask, completing the device structure under strain. Electrical measurements were carried out using a Keithley 4200-SCS and 2600B semiconductor parameter analyzer in a nitrogen atmosphere. Transfer characteristics were recorded by sweeping the V_G from −20 to 100 V at a fixed V_{DS} of 100 V. Charge carrier mobilities were extracted from the linear regime of the transfer curves.

3. Results and discussion

3.1 Design and characterization of CBS-based polymers

This study focuses on the design and synthesis of stretchable n-type semiconducting polymers incorporating structurally distinct alicyclic CBSs to elucidate their impact on polymer morphology and the trade-off between mobility and stretchability. The CBSs employed in this study include a tricyclic diol, a mixture of tricyclic diol isomers, and a monocyclic diol, enabling systematic variation in ring complexity, symmetry, and rigidity. The synthetic routes of the CBSs are shown in Scheme 1. All CBSs were synthesized *via* Steglich esterification using 4-bromobenzoic acid. The *r*TCDs–CBS and *t*CH–CBS were synthesized in a single step from the corresponding commercially available tricyclodecanedimethanol and *trans*-1,4-cyclohexanediol. Unlike *r*TCDs–CBS, synthesized *via* rhodium-catalyzed hydrohydroxymethylation of DCPD under CO/H_2 to yield an isomeric mixture,[34,35] TCD–CBS is obtained through a completely different route involving hydrogenation of Thiele's acid. In this pathway, deprotonated DCPD reacts with CO_2 to form Thiele's acid, which is then hydrogenated. Due to steric hindrance on the endo side of the polycyclic scaffold, hydrogenation occurs exclusively from the exo face.[39] As a result, both carboxylic acid groups are oriented toward the endo face, yielding the unique all-endo TCD–diacid, which is then reduced to TCD–diol and subsequently esterified with 4-bromobenzoic acid.[36] This distinction explains the absence of **TCD** in the isomeric mixture of ***r*TCDs**. The chemical structures of the synthesized CBSs were confirmed by ^1H and ^{13}C NMR, and elemental analyses (see the Experimental section and SI). Notably, the absence of TCD–CBS in the *r*TCDs–CBS mixture was further confirmed by ^1H NMR analysis, as shown in Fig. 1. The methylene protons between tricyclodecane and ester group display distinct ^1H NMR signals, ranging from 4.1–4.3 ppm for the former and 4.3–4.5 ppm for the latter.

Scheme 1 and the Experimental section provide the full synthetic procedures for the NDI-based terpolymers incorporating CBSs. The corresponding NDI-based terpolymers were synthesized *via* Migita–Kosugi–Stille coupling polymerization using Br–NDI–Br, 2T, and each CBS. A consistent molar ratio of NDI to CBS (80 : 20) was employed for all reactions. A summary of these parameters is provided in Table S1. The actual CBS content in the resulting polymers, calculated from the integration of characteristic

NMR proton peaks, was found to be 13, 13, and 17 mol% for **TCD**, ***r*TCDs**, and ***t*CH**, respectively, as shown in Fig. S5–S10. The resulting polymers exhibited M_n ranging from 20 400–26 200, with $Đ_M$ values between 2.30–4.40, as determined by SEC UV traces in Fig. S11. To evaluate the effect of CBS incorporation and structural complexity, a reference polymer, **PNDI2T**, which lacks any CBS component, was also synthesized for comparison.

3.2 Thermal properties of the conjugated polymers

The thermal characteristics of the synthesized polymers were evaluated by TGA and DSC, with results presented in Fig. S12. A summary of the thermal decomposition ($T_d^{5\%}$), melting temperatures (T_m), and glass transition temperature (T_g) can be found in Table S1. The measured $T_d^{5\%}$ values were 317, 441, and 429 °C for **TCD**, ***r*TCDs**, and ***t*CH**, respectively, compared to 447 °C for **PNDI2T**.[40] The consistently lower $T_d^{5\%}$ values observed in all CBS-containing polymers suggest that the introduction of CBS units reduces thermal stability, likely due to their conformational freedom and interruption of π–conjugation, which create thermally weaker sites along the backbone. While the symmetric, monocyclic structure of ***t*CH** may inherently suppress thermally labile sites that enhance stability, the higher $T_d^{5\%}$ of ***r*TCDs** compared to pure **TCD** can be attributed to the thermodynamic and structural characteristics of the *endo*/*exo* tetrahydrodicyclopentadiene (THDCPD) framework, which shares the same rigid tricyclic norbornane skeleton as TCD–CBS and *r*TCDs–CBS. DFT calculations indicate that *exo*-THDCPD is approximately 15.5 kJ mol^{-1} more stable than the *endo* isomer, consistent with its lower gas-phase enthalpy of formation.[41,42] This enhanced stability arises from the flipping of the g–h–i triangular ring in the norbornane skeleton, which induces steric strain in the endo configuration. In *endo*-THDCPD, certain C–C bonds are elongated due to through-space interactions, indicating higher ring strain that generally reduces thermal stability by weakening bonds and making them more reactive. Moreover, studies have reported that *exo*-THDCPD exhibits a larger HOMO–LUMO gap, suggesting greater stability and lower reactivity under thermal or oxidative conditions.[42] As ***r*TCDs** contain a mixture of *exo* and *endo* isomers, they benefit from both the lower intrinsic reactivity and the stabilizing configurational effect of the *exo* form, collectively suppressing early decomposition and imparting greater thermal robustness compared to the pure *endo*-configured **TCD**. Melting transitions were observed at 285 and 276 °C for ***r*TCDs** and ***t*CH**, respectively. **PNDI2T**, with a comparable M_n, has been reported to exhibit a higher T_m of 301 °C,[43] reflecting its rigid, planar backbone that enables dense crystalline packing compared to CBS-containing counterparts. In contrast, the higher T_m of ***r*TCDs** relative to ***t*CH** suggests that, despite isomeric irregularity, the bulky tricyclic structure promotes partial packing regularity. In contrast, the flexible monocyclic structure limits the formation of ordered domains. To further quantify and interpret thermal transition behavior, the enthalpies of fusion (ΔH_f) for ***r*TCDs** and ***t*CH** were calculated to be 2.93 and 3.37 J g^{-1}, respectively. At the same time, **PNDI2T** was reported to have a ΔH_f of 3.95 J g^{-1}.[43] Corresponding entropies of fusion (ΔS_f), derived using the relation $\Delta S_f = \Delta H_f / T_m$, were determined to be 5.20, 6.14, and 6.88 mJ g^{-1} K^{-1} for ***r*TCDs**, ***t*CH**, and **PNDI2T**, respectively. The lower ΔS_f values observed for CBS-containing polymers suggest that the presence of alicyclic moieties increases chain flexibility and reduces packing rigidity, thereby introducing more free volume and enhancing mechanical compliance. Notably, ***r*TCDs** exhibited the lowest ΔS_f, likely due to isomeric irregularities that disrupt long-range crystalline order. This partial disorder increases the amorphous content without compromising local regularity, enabling a balance between structural flexibility and sufficient molecular order for effective charge transport. In addition, their thermomechanical behavior was further evaluated using DMA, as shown in Fig. S13 and Table S1. Glass transition temperatures were measured at 69, 65, and 72 °C for **TCD**, ***r*TCDs**, and ***t*CH**, respectively. The elevated T_g of ***t*CH** is attributed to its symmetric monocyclic structure, which minimizes steric hindrance and promotes tighter chain packing, effectively restricting segmental motion. In contrast, the bulky tricyclic structure in **TCD** and ***r*TCDs** introduces significant steric hindrance that disrupts compact packing in disordered regions. Building upon this structural constraint, the isomeric irregularity in ***r*TCDs** likely generates more amorphous domains and increases free volume, resulting in a lower T_g. The implications of this thermal behavior on polymer morphology will be discussed in the following section.

3.3 Optical, aggregation, and electrochemical characterizations

Fig. 2a presents the UV-vis absorption spectra of the polymer thin films. All polymers exhibit dual absorption features, with π–π* electronic transitions occurring in the 300–450 nm range and intramolecular charge transfer (ICT) observed in the 500–800 nm region. Maximum absorption peaks (λ_{max}) were observed at (396, 699) nm, (394, 695) nm, (394, 689) nm, and (393, 702) nm for **TCD**, ***r*TCDs**, ***t*CH**, and **PNDI2T** respectively. **PNDI2T** shows a more distinct red shift compared to its CBS-containing counterparts, which can be attributed to its fully conjugated, rigid, and planar backbone. Among the CBS polymers, the pronounced red shift in **TCD** and ***r*TCDs** compared to ***t*CH** is likely attributed to their tricyclic structures, which promote more planar conformations and facilitate stronger intermolecular π–π interactions, thereby enhancing solid-state aggregation. Variations in the 0–0/0–1 vibrational ICT peak intensity were also observed, with absorbance ratios of 0.74, 0.73, 0.68, and 0.83 for **TCD**, ***r*TCDs**, ***t*CH**, and **PNDI2T**, respectively. As expected, **PNDI2T** shows the highest ratio, reflecting its rigid, fully conjugated backbone that favors strong intrachain planarity and aggregation. For the CBS-containing polymers, the higher ratios in **TCD** and ***r*TCDs** indicate more ordered packing and improved intrachain planarity that promote

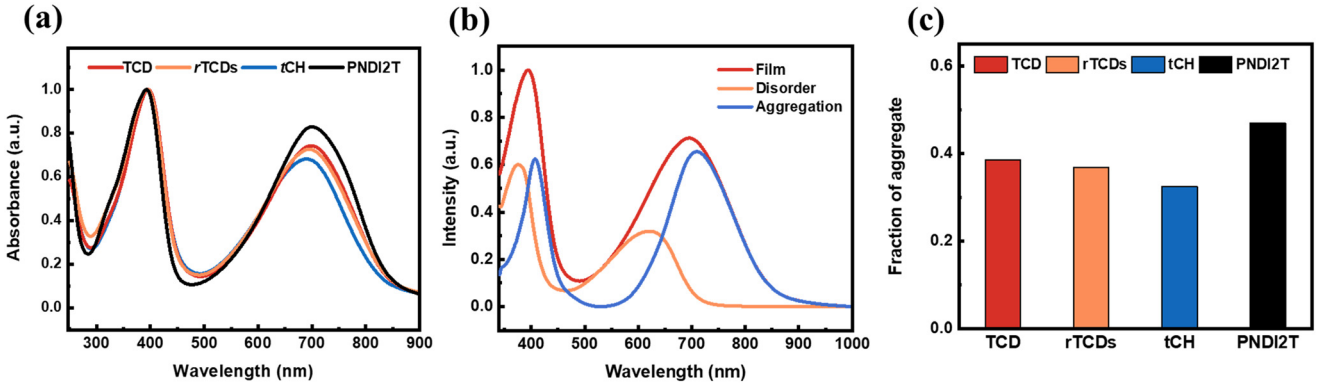

Fig. 2 (a) UV-vis absorption spectra of the polymer films. (b) Spectral deconvolution of ***r*TCDs**, separating aggregated and disordered contributions in the thin film state. (c) Quantitative comparison of aggregation fractions among the polymer films.

short-range aggregation. In contrast, the lower ratio observed in ***t*CH** reflects the tendency of its monocyclic structure to hinder aggregation and disrupt the formation of locally ordered domains in the solid state. The slightly reduced aggregation observed for ***r*TCDs** compared to **TCD** may result from the structural complexity of the isomeric mixture, which could weaken uniform molecular packing. To quantify these differences, the UV-vis absorption spectra of the polymer films were deconvoluted into aggregated and disordered components, as shown in Fig. 2b and S14. The solution-state absorption spectrum in 1-chloronaphthalene was used as a reference to represent the disordered state, and the calculation method for aggregation fractions is detailed in the SI. Corresponding aggregation fractions are shown in Fig. 2c and summarized in Table S2. The calculated aggregation fraction of the polymer films was 0.39, 0.37, 0.32, and 0.47 for **TCD**, ***r*TCDs**, ***t*CH**, and **PNDI2T**, respectively, consistent with the trend observed in their 0–0/0–1 absorbance ratio. These disparities in aggregation behavior may contribute to the differences in FET device performance

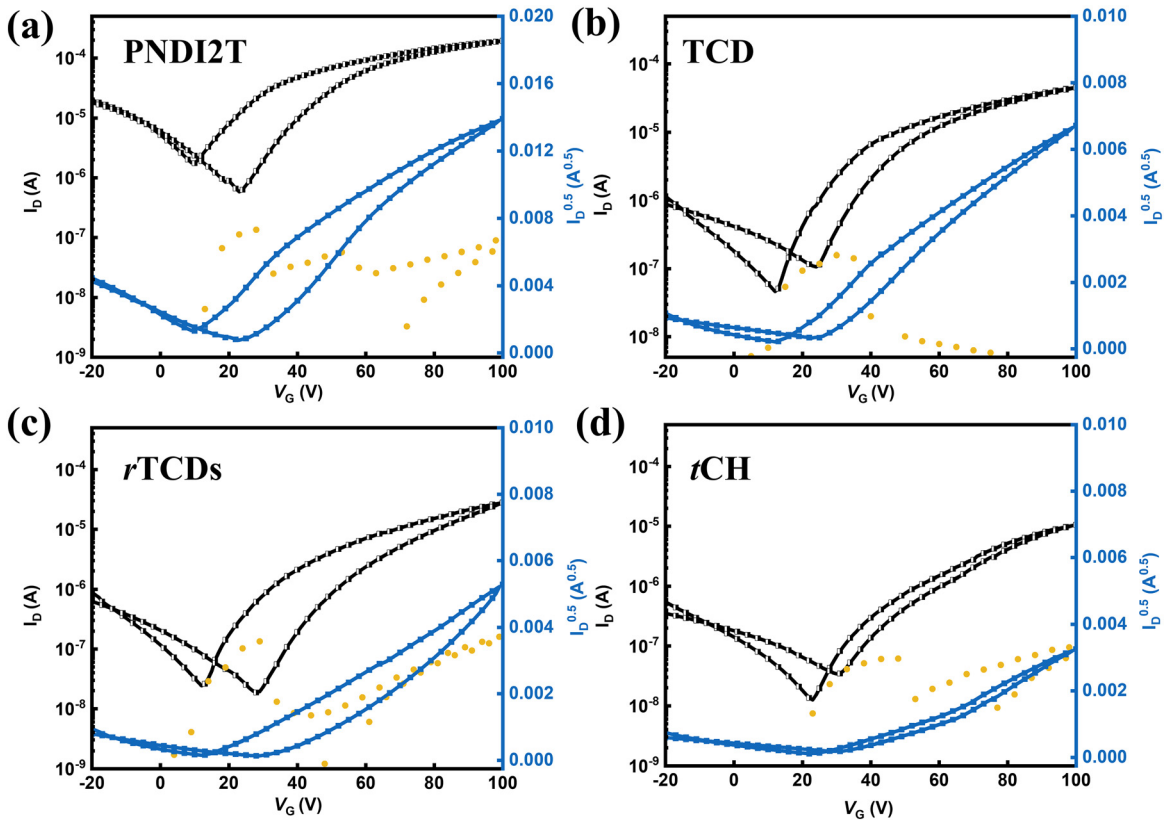

Fig. 3 Transfer characteristics of the pristine FET devices: (a) **PNDI2T**, (b) **TCD**, (c) ***r*TCDs**, and (d) ***t*CH** films. The yellow scatter points following the left *y*-axis represent the gate current measured during V_G sweeps from −20 to 100 V under a fixed V_{DS} of 100 V.

discussed later. To further investigate the electronic properties of the polymers, the highest occupied and lowest unoccupied molecular orbital (HOMO/LUMO) levels were estimated from the optical bandgaps (E_g) derived from UV-vis absorption spectra and the oxidative onset potentials obtained from CV measurements, as shown in Fig. S15 and Table S1. All polymers exhibited nearly identical energy levels, with HOMO and LUMO values around −6.04 ± 0.02 eV and −4.16 ± 0.02 eV, respectively. This uniformity suggests that variations in alicyclic ring size and structural complexity have little effect, as the NDI-based conjugated backbone predominantly governs the energy levels.

3.4 FET device characteristics

To evaluate the charge transport behavior of the synthesized polymers, bottom-gate, top-contact FET devices were fabricated and characterized. The fabrication process began with spin-coating polymer solutions onto ODTS-modified silicon wafers, followed by thermal annealing. Gold electrodes were subsequently deposited through a shadow mask to define the source and drain contacts. Detailed fabrication procedures are described in the Experimental section. The transfer and output characteristics of the annealed devices are shown in Fig. 3 and S16, while key performance metrics such as electron mobility (μ_e), on/off current ratio (I_{on}/I_{off}), and threshold voltage (V_{th}) are summarized in Table 1. All polymers demonstrated typical n-type transfer characteristics, with μ_e values of 0.080, 0.058, 0.029, and 0.32 $cm^2\ V^{-1}\ s^{-1}$ for annealed **TCD**, ***r*TCDs**, ***t*CH**, and **PNDI2T**, respectively. Among them, **PNDI2T**, which lacks CBSs, showed the highest electron mobility. While this superior mobility reflects a highly ordered crystalline phase, as indicated by elevated ΔS_f and T_m values, the resulting structural rigidity may limit its mechanical adaptability under strain. In contrast, polymers incorporating CBSs exhibited slightly reduced mobility but good I_{on}/I_{off} ratios, with values reaching approximately 10^4. The CBS incorporation disrupts long-range crystalline order and reduces the size of crystalline domains, leading to improved morphological uniformity. Among these, **TCD** displayed the highest μ_e among the CBS-containing polymers, while ***t*CH** exhibited the lowest. This trend aligns with their aggregation behavior observed in UV-vis absorption spectra, where **TCD** exhibited the most substantial degree of chain aggregation. The lower mobility of ***r*TCDs** compared to **TCD** implies that isomeric structure can disrupt aggregation and impair transport. Nevertheless, both **TCD** and ***r*TCDs** outperformed ***t*CH**, highlighting the beneficial effect of the rigid tricyclic ring in promoting molecular aggregation. Additional morphological factors such as film crystallinity, lamellar ordering, and roughness are also expected to impact charge transport performance and will be discussed in the following sections.

3.5 Morphological characterizations of the polymer thin films

To investigate how structural variations in the CBS units influence device performance, the surface morphology of the polymer films was examined by tapping-mode AFM. As shown in Fig. 4a–c, the thermally annealed films exhibited root-mean-square roughness values of 1.60, 1.51, and 1.29 nm for **TCD**, ***r*TCDs**, and ***t*CH**, respectively, while a reported value of 0.86 nm was obtained for **PNDI2T**.[40] Polymers containing tricyclic spacers exhibited more pronounced surface features compared to the smoother morphology observed in the monocyclic system. This trend is consistent with UV-vis absorption results, which suggest that rigid and bulky tricyclic structures promote stronger interchain aggregation, thereby contributing to enhanced mobility. However, between the two tricyclic systems, ***r*TCDs** exhibit lower surface roughness than **TCD**, likely due to structural irregularities that disrupt regular chain packing and hinder the formation of extended crystalline domains. This irregularity suppresses large-scale aggregation, leading to a more homogeneous film morphology. In contrast, **PNDI2T**, with its fully conjugated backbone free of CBS units, forms a highly ordered and uniform molecular arrangement that minimizes topographic variation, resulting in the smoothest films.

While AFM provides insights into surface morphology, grazing-incidence wide-angle X-ray scattering (GIWAXS) was employed to assess the crystallinity and molecular orientation of the polymer films. Fig. 4d–f displays the 2D GIWAXS patterns, and Fig. S17–S19 show the corresponding 1D line profiles extracted along the out-of-plane (OOP) and in-plane (IP) directions, along with pole figures derived from (100) reflections. Fig. S30 summarizes the relative degree of crystallinity (rDOC), determined from the OOP (100)

Table 1 Summary of the FET and GIWAXS parameters of the polymer films

	μ_e[a] ($cm^2\ V^{-1}\ s^{-1}$)	I_{on}/I_{off}	V_{th} (V)	R_q[b] (nm)	$d_{lamellar}$[c] (Å)	FWHM ($Å^{-1}$)	L_c[d] (Å)	g	Edge-on population[e]
***r*TCDs**	0.058 ± 0.019	6.7×10^4	13	1.51	24.1	0.083	67.8	0.226	0.411
TCD	0.080 ± 0.012	4.9×10^4	11	1.60	23.4	0.072	78.1	0.207	0.260
***t*CH**	0.029 ± 0.010	3.7×10^4	18	1.29	23.7	0.052	108.2	0.177	0.625

[a] Electron mobility (μ_e) was averaged over 15 devices fabricated across three independent batches and measured in a nitrogen-filled glovebox. [b] The root-mean-square surface roughness of the AFM height images. [c] Lamellar spacing was obtained from the (100) diffraction peaks measured in the (OOP) direction. [d] Coherence length was estimated using the Scherrer equation based on the FWHM of the (100) OOP diffraction peaks. [e] The edge-on orientation fraction was derived from the ratio of OOP to total (OOP + IP) scattering intensities in the geometrically corrected pole figures.

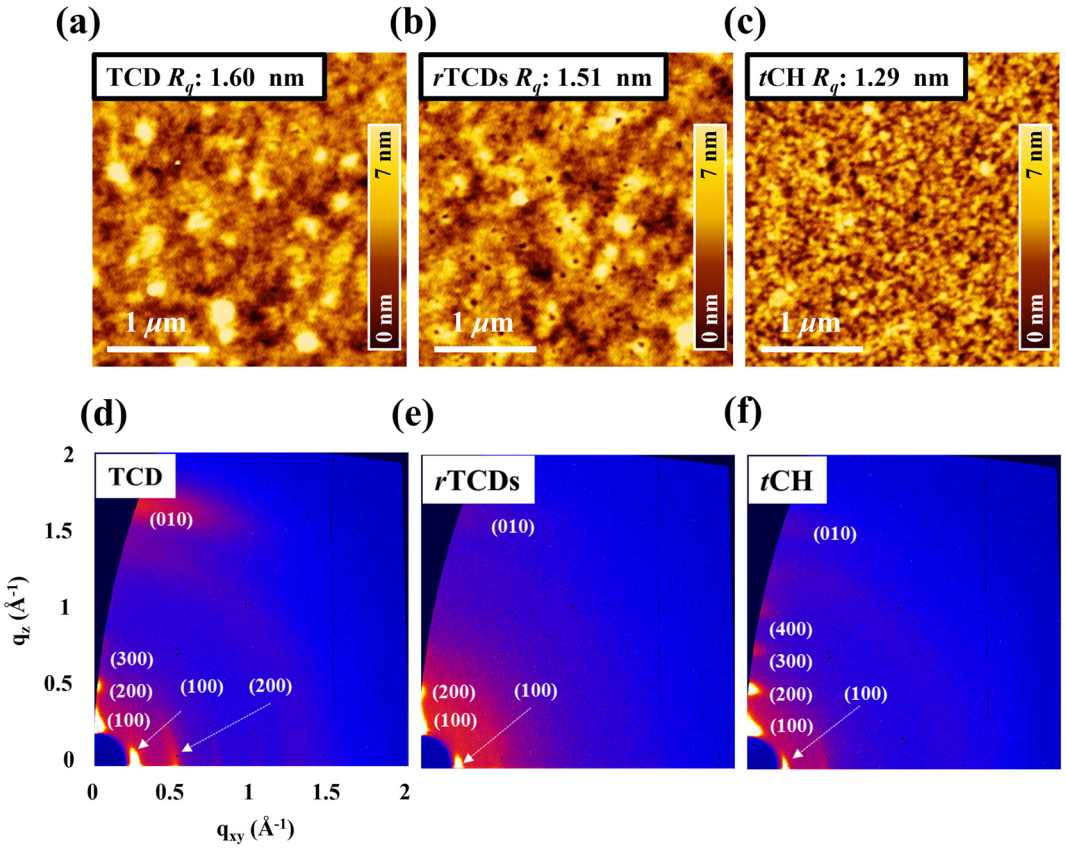

Fig. 4 AFM topographies of the (a) **TCD**, (b) ***r*TCDs**, and (c) ***t*CH** films. (b) 2D diffraction patterns from GIWAXS of the (d) **TCD**, (e) ***r*TCDs**, and (f) ***t*CH** films. These pristine films were characterized without film transfer and stretching.

diffractions of the polymer films. Key crystallographic parameters, including the lamellar spacing (d_{lamellar}), crystalline coherence length (L_c), paracrystalline disorder (g), and orientation population, were calculated and are summarized in Table 1. The paracrystalline disorder was calculated using the formula $g = [0.5 \times \text{FWHM}/(\pi q)]^{0.5}$, and the edge-on population was obtained from pole figures with geometric correction. GIWAXS analysis revealed that **TCD** and ***t*CH** films predominantly adopt face-on and edge-on orientations, with edge-on populations of 26% and 63%, respectively. In contrast, ***r*TCDs** exhibit a mixed alignment comprising approximately 41% edge-on orientations. Relative to the reported **PNDI2T** reference, the rDOC values decrease to 83%, 43%, and 29% for ***t*CH**, ***r*TCDs**, and **TCD**, respectively.[40] This reduction in crystallinity reflects the expansion of amorphous domains, which enhances ductility and highlights greater backbone flexibility introduced by CBS units. Measured d_{lamellar} values were 23.44, 24.10, and 23.70 Å for **TCD**, ***r*TCDs**, and ***t*CH**, respectively, with corresponding g values of 0.207, 0.226, and 0.177. Reported value of d_{lamellar} and g for **PNDI2T** are 25.2 Å and 0.115, respectively.[40] The absence of CBS has been found to give rise to a larger lamellar spacing and lower g, owing to the fully conjugated and planar backbone. Among three CBS incorporated polymers, the rigid tricyclic structure in **TCD** promotes planar chain conformation and short-range aggregation, enabling tight lamellar stacking in the OOP direction while limiting structural relaxation during film formation. In contrast, ***t*CH** exhibits greater conformational freedom due to its flexible monocyclic structure, which reduces packing density but retains stacking continuity. In contrast, the slightly larger d_{lamellar} in ***r*TCDs** may arise from steric repulsion and spatial irregularity introduced by isomeric structure. This behavior is also reflected in the g values, where tricyclic moieties have demonstrated higher disorder compared to monocyclic ***t*CH**. The symmetric and flexible structure of ***t*CH** facilitates better steric compatibility, enabling longer-range crystalline coherence despite increased interchain spacing. Interestingly, ***r*TCDs** exhibit the highest g value among the three, likely due to isomeric irregularity that disrupts uniaxial packing, increases interchain spacing, and hinders the development of extended crystalline domains. Although structural disorder is typically detrimental to charge transport, the elevated g value in ***r*TCDs** is attributed to its bimodal molecular orientation, which contributes positively to carrier conduction. This mixed face-on and edge-on configuration has been shown to provide more continuous and isotropic pathways for carriers hopping across grain boundaries and disordered regions, thereby enhancing overall charge conduction.[44,45] Such bimodal orientation supports the three-dimensional (3D) nature of charge transport in polymer films by facilitating efficient carrier movement along both IP and

OOP directions. Although ***r*TCDs** shows slightly lower μ_e than **TCD**, their disrupted packing introduces free volume and alleviates local stress concentration, making them a promising candidate for improved mechanical compliance and stretchability. This aspect will be further discussed in the following section. Overall, the isomeric structure of ***r*TCDs** is expected to yield better mechanical stretchability while maintaining its μ_e through bimodal orientation.

3.6 Morphological characterization of the stretched films

To investigate the morphological transformation of polymer films under strain, OM and AFM analyses were performed on thermally annealed samples subjected to varying strain levels. The corresponding OM images and AFM topographies are presented in Fig. 5a and b. Distinct differences in crack onset and surface morphology were observed among the different alicyclic spacers. The simple and flexible structure of ***t*CH** has been found to withstand strain up to 20% before crack formation. In contrast, both **TCD** and ***r*TCDs**, featuring tricyclic structures, exhibited earlier crack onset at strains between 10% and 20%. This consistent trend observed in both OM and AFM images highlights the influence of backbone rigidity on the mechanical resilience of the polymer films.

Building upon morphological observations, tensile mechanical testing was performed to quantify the intrinsic stiffness of the polymer films following the film-on-thin-elastomer method.[46,47] Polymer films approximately 50 nm thick were transferred onto thin PDMS substrates (~10 μm thickness) to form bilayer laminates, and their stress–strain behaviour was subsequently analyzed. The raw stress–strain curves of the bilayers are shown in Fig. S20. At the same time, the corrected polymer responses obtained by subtracting the contribution of the PDMS layer are presented in Fig. 5c and summarized in Table S3. The calculated elastic moduli were 262, 106, and 74 MPa for **TCD**, ***r*TCDs**, and ***t*CH**, respectively, compared with a reported value of 720 MPa for **PNDI2T**.[40] As expected, polymers without CBS exhibited the highest stiffness owing to their rigid, crystalline, and fully conjugated backbones, which resist deformation. By contrast, CBS-containing polymers showed reduced stiffness, with the rigid tricyclic structure imparting a greater modulus than the flexible monocyclic ***t*CH**. Notably, despite both containing tricyclic moieties, a pronounced difference in modulus was observed between **TCD** and ***r*TCDs**. This discrepancy is attributed not only to the stronger aggregation and denser packing of **TCD** but also to the disrupted chain organization caused by the isomeric structure in ***r*TCDs**, which reduces stiffness. These findings underscore the combined impact of

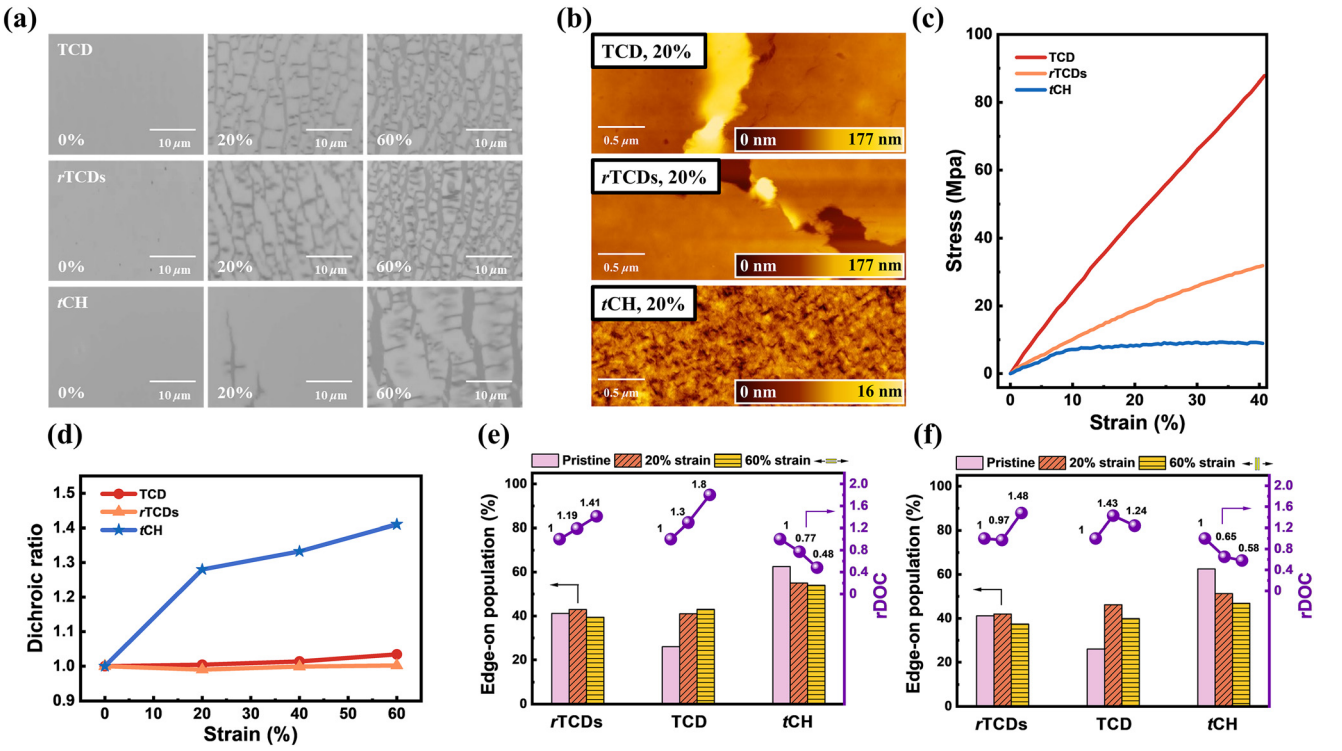

Fig. 5 (a) Optical microscopy images of polymer films on PDMS substrates at different strain levels, illustrating morphological evolution. (b) AFM surface profiles under 20% strain. (c) Stress–strain behaviors of the polymer thin films. (d) The calculated dichroic ratios of the stretched films derived from the polarized UV-vis absorption spectra. Strain-induced changes in relative crystallinity (rDOC) and edge-on orientation, extracted from OOP and IP (100) diffraction patterns measured with the incident beam oriented (e) perpendicular and (f) parallel to the strain direction in three polymer films.

ring rigidity and structural complexity on the mechanical properties of conjugated polymers.

While morphological observations provide evidence of mechanical behavior, they offer limited insight into molecular-scale alignment. To bridge this gap and correlate surface morphology with molecular orientation under deformation, we analyzed the dichroic ratios of the strained polymer films, defined as the ratio of polarized absorbance ($A^{\parallel}/A^{\perp}$) with incident light polarized parallel and perpendicular to the strain direction. These values, derived from the polarized UV-vis spectra in Fig. S21 and summarized in Fig. 5d, reflect the extent of chain orientation along the applied strain. At 20% and 60% strains, the dichroic ratios were (1.00, 1.03), (0.99, 1.00), and (1.28, 1.41) for **TCD**, ***r*TCDs**, and ***t*CH**, respectively, compared to (1.11, 1.82) for **PNDI2T**.[40] Among all polymers, **PNDI2T** exhibited significantly higher dichroic ratios, attributable to its rigid, planar backbone that resists coiling or entanglement and is thus compelled to align along the strain direction. Within the CBS-containing polymers, ***t*CH** showed the most pronounced increase in chain alignment with strain, reflecting its enhanced chain conformability and flexibility. In contrast, the rigid tricyclic structures of **TCD** and ***r*TCDs** likely limit conformational freedom and promote π–π stacking, thereby restricting reorientation under stress and contributing to enhanced structural stability during deformation. This behavior is favorable for achieving an isotropic mobility–stretchability relationship.

Moreover, to further reveal differences in crystallinity among the polymers, GIWAXS investigation was employed to elucidate the relationship between morphology and microstructure under deformation. The population orientation, rDOC, and 2D GIWAXS patterns of the strained films are shown in Fig. 5e, f, S22, and S23. Corresponding 1D GIWAXS line profiles extracted along the OOP and IP directions are presented in Fig. S17 and S18, while geometrically corrected pole figures based on the (100) reflections are provided in Fig. S19. Key crystallographic parameters, molecular orientation populations, and rDOC are summarized in Tables S4–S7. As mentioned earlier, the estimated edge-on populations in the pristine state were 26%, 41%, and 62% for **TCD**, ***r*TCDs**, and ***t*CH**, respectively. Upon applying 20% and 60% strain, these values evolved to (41, 43)%, (43, 40)%, (55, 54)%, perpendicular to the channel direction and (46, 40)%, (42, 37)%, (51, 47)% parallel to the channel direction, respectively. In terms of crystallinity, the rDOC values at (0, 20, 60)% strains of **TCD**, ***r*TCDs**, and ***t*CH** are (1, 1.3, 1.8), (1, 1.2, 1.4), (1, 0.8, 0.5) perpendicular to the channel and (1, 1.4, 1.2), (1, 1, 1.5), (1, 0.7, 0.6) parallel to the channel, respectively. The degradation observed in ***t*CH** likely originates from its inherently soft and flexible backbone, which facilitates chain conformability but results in an unstable microstructure and strain-sensitive crystallinity. In contrast, tricyclic moieties such as **TCD** and ***r*TCDs** exhibit enhanced rDOC under strain, indicating improved crystalline order. Although both polymers show increased rDOC, ***r*TCDs** display a more stable evolution, where moderate isomeric disorder acts as a buffer against mechanical deformation. This isomeric feature enables local chain adaptability without significant alteration of textural order or crystalline coherence, revealing its potential for delivering isotropic and strain–resilient charge transport in stretchable electronics.

3.7 Mobility–stretchability of the polymer films under tensile strains

To investigate the interplay between mechanical deformation and charge transport, the mobility–stretchability characteristics of the polymers were evaluated through film-transfer FET devices. Polymer films were first stretched and transferred onto silicon wafers, followed by the deposition of gold electrodes *via* shadow masking to define the channel. Strain was applied either parallel (∥) or perpendicular (⊥) to the charge transport direction. Fig. 6a and b present the transfer curves at 40% strain in both directions, while Fig. 6c and d summarize the evolution of electron mobility under strain. The transfer and output characteristics of the stretched devices are presented in Fig. S24–S26, while the corresponding device parameters are summarized in Table S8. At 0% strain, the averaged μ_e of **TCD**, ***r*TCDs**, and ***t*CH** were 0.0183, 0.0242, and 0.0050 $cm^2\ V^{-1}\ s^{-1}$, respectively. As strain increased to 20%, 40%, and 60%, the averaged $\mu_e^{\perp}$ were (0.0159, 0.0064, 0.0030), (0.0210, 0.0114, 0.0065), and (0.0063, 0.0053, 0.0026) $cm^2\ V^{-1}\ s^{-1}$; whereas $\mu_e^{\parallel}$ had varied to (0.0093, 0.0016, 0.0004), (0.0078, 0.0028, 0.0018), and (0.0055, 0.0035, 0.0014) $cm^2\ V^{-1}\ s^{-1}$. Directional uniformity, quantified by the $\mu_e^{\parallel}/\mu_e^{\perp}$ ratio at 60% strain, yielded values of 0.12, 0.28, and 0.52 for **TCD**, ***r*TCDs**, and ***t*CH**, respectively. These results reveal distinct transport behaviors across the polymer series. ***t*CH** maintains relatively isotropic transport; however, its overall performance is limited by weak intermolecular aggregation and low intrinsic mobility. In contrast, **TCD** exhibits high initial mobility due to its rigid and symmetric structure, but its performance rapidly declines in the parallel direction under strain, indicating poor mechanical resilience. Among all polymers, ***r*TCDs** exhibit the most favorable balance between charge transport and mechanical adaptability, maintaining both relatively high electron mobility and moderate isotropy under increasing strain. This behavior is primarily attributed to microstructural disorder arising from its isomeric composition, which induces stable orientation under strain. Such packing relaxes chain alignment constraints and suppresses anisotropic mobility degradation, enabling more uniform charge transport in both IP and OOP directions. Furthermore, the combination of enhanced π–π stacking interactions and reduced crystalline domain size contributes to a more compliant microstructure, supporting a superior mobility–stretchability trade-off.

To verify the inferred isotropic and stable charge transport of ***r*TCDs** under repeated strain, stretch–release cycling tests were conducted at 40% strain to evaluate mechanical durability

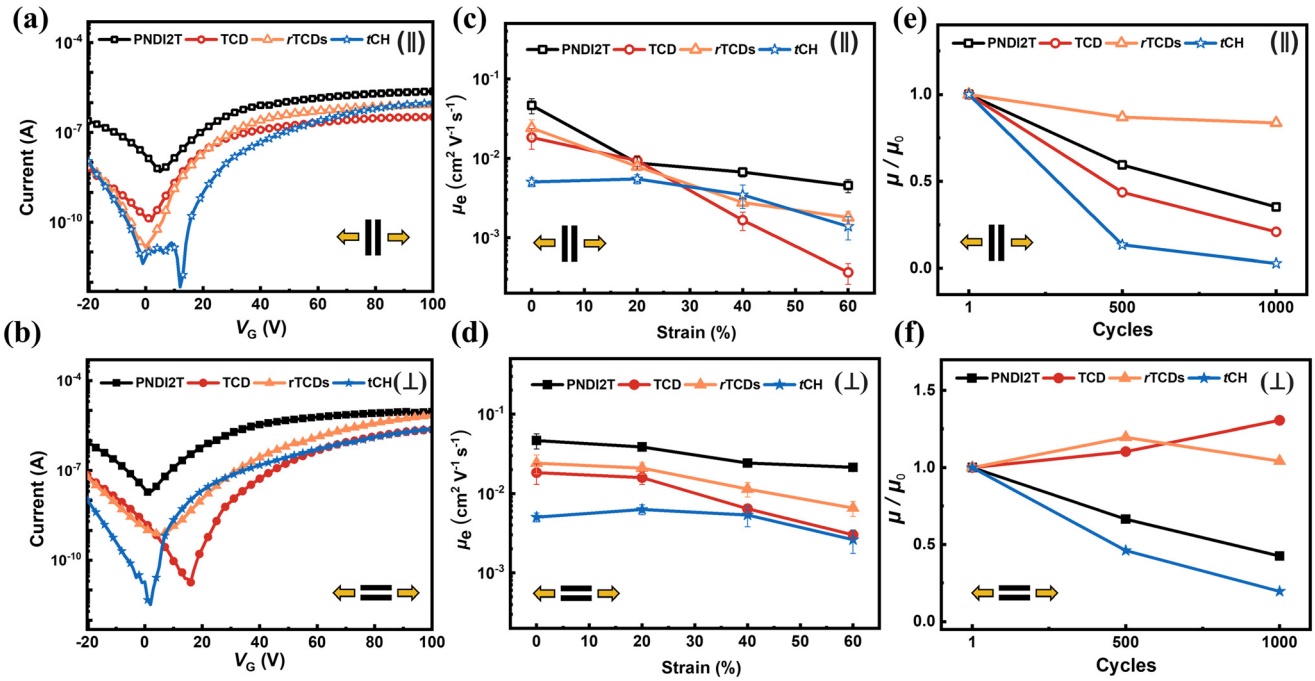

Fig. 6 (a and b) Transfer characteristics under 40% strain, (c and d) mobility variation as a function of applied strain, and (e and f) mobility retention over stretch–release cycles relative to a single cycle at 40% strain, measured with strain applied (a, c and e) parallel and (b, d and f) perpendicular to the channel direction.

and retention of directional mobility. Electrical performance was evaluated through transfer characteristics, as shown in Fig. S27 and S28. The evolution of μ_e retentions and μ_e values along the parallel and perpendicular directions is illustrated in Fig. 6e, f and S29. After 500 cycles, the ($\mu_e^{\perp}$, $\mu_e^{\parallel}$,) values were for **TCD**, ***r*TCDs**, and ***t*CH** were (0.0071, 0.0007), (0.0135, 0.0022), and (0.0025, 0.0005) cm^2 V^{-1} s^{-1}, respectively. By 1000 cycles, their ($\mu_e^{\perp}$, $\mu_e^{\parallel}$) values had shifted to (0.0084, 0.0004), (0.0118, 0.0021), and (0.0010, 0.0001) cm^2 V^{-1} s^{-1} for **TCD**, **rTCDs**, and **tCH**, respectively. Among them, ***r*TCDs** maintained the most stable values for both $\mu_e^{\perp}$ and $\mu_e^{\parallel}$, reflecting their superior mechanical resilience and isotropic charge transport during repeated deformation. In contrast, $\mu_e^{\parallel}$ in **TCD** and ***t*CH** showed a continued decline, indicative of directional degradation. Interestingly, a slight increase in $\mu_e^{\perp}$ was observed for **TCD**, possibly due to strain-induced chain alignment or crystallite reorganization perpendicular to the transport direction. While both **TCD** and ***t*CH** suffer from direction-dependent degradation under cyclic strain, their underlying failure mechanisms differ. In **TCD**, the rigid and planar backbone limits stress dissipation and promotes the accumulation of surface defects, which in turn encourages anisotropic chain orientation and leads to a gradual reduction in $\mu_e^{\parallel}$. ***t*CH**, on the other hand, exhibits a sharp decline in mobility due to microstructural collapse; its flexible backbone fails to maintain π–π stacking during repeated deformation, thereby disrupting charge transport pathways. While OM images suggest that ***r*TCDs**-based films may exhibit more visible cracks than ***t*CH** under strain, the relative stretchability (rS) analysis, which is defined as the change of polymer chain alignment (dichroic ratio) over the change of relative degree of crystallinity (rDOC) as a function of strain, provides a more direct measure of a film's ability to sustain charge transport.[48] For ***r*TCDs** (rS = −0.06), the small negative value indicates the presence of strain-induced crystallization (SIC), meaning that the strain response is governed by a balance between minor amorphization and SIC rather than extensive crystalline loss. By contrast, ***t*CH**, with a low rS of 0.77, exhibits net amorphization of crystallites. While this modest chain alignment may delay crack formation, the dominant amorphization directly compromises the charge transport network, leading to reduced mobility. Thus, the apparent discrepancy between OM crack density and electrical stability can be reconciled in systems such as ***r*TCDs**, as the underlying transport network remains mechanically and morphologically resilient. Based on these findings, ***r*TCDs** overcome these limitations through their unique isomeric structure. The structural disorder inhibits significant change in crystallinity and introduces free volume, enhancing ductility while maintaining sufficient molecular packing. Moreover, the emergence of a bimodal orientation facilitates isotropic charge transport, minimizing direction-dependent failure. This combination of mechanical compliance and morphological stability enables ***r*TCDs** to retain balanced $\mu_e^{\perp}$ and $\mu_e^{\parallel}$ values over extended cycling, demonstrating superior durability and isotropic transport behavior compared to their more rigid or overly flexible counterparts.

To benchmark these materials, their performance was compared to that of the reference polymer **PNDI2T**, which lacks CBS units. Although both **TCD** and ***t*CH** exhibited

Table 2 Comparative summary of stretchable FET performance in this work and the recent reports concerning the mobility–stretchability relationship and the corresponding isotropic stability after stretch–release cycles

Type	Backbone	Polymer	μ_0[a] ($cm^2\ V^{-1}\ s^{-1}$)	$\mu_{60}^{\parallel}/\mu_{60}^{\perp}$[b]	$\mu_{cycle}^{\parallel}/\mu_{strain}^{\parallel}$[c]	$\mu_{cycle}^{\perp}/\mu_{strain}^{\perp}$[c]	Ref.
N-type	NDI	*r*TCDs	0.0242	0.27	0.77	1.04	This work
N-type	NDI	ABA52[d]	0.0032	0.90	3.42	0.77	49
N-type	NDI	P3[e]	0.01	0.24	0.50	2.86	50
N-type	NDI	ISB[f]	0.0052	1.18	0.40	1.21	25
N-type	DPP	DPP[g]	0.001	2.11	0.08	0.14	26
N-type	TIC	s-PCDT-TIC[h]	0.00028	1.45	—	—	51
P-type	DPP	P2[i]	1.063	3.39	0.84	0.43	32

[a] Mobility measured under 0% strain. [b] Mobility isotropy ratio evaluated at 60% strain. [c] Mobility retention after final stretch–release cycles at each applied strain, calculated as the ratio to the corresponding single-cycle performance, with channels oriented parallel and perpendicular to the strain direction. [d] Triblock copolymers comprising polyisobutene–*block*–PNDI2T–*block*–polyisobutene. [e] Random copolymers comprising poly(naphthalene diimide-*alt*-(thiophene-vinylene-thiophene-*ran*-thiophene-imine-thiophene)). [f] **PNDI2T** randomly copolymerized with an isosorbide-based CBS. [g] Poly(diketopyrrolopyrrole-*alt*-bithiophene) randomly copolymerized with non-centrosymmetric spiro[cycloalkane-1,9′-fluorene] spacers. [h] Poly(cyclopentadithiophene-*alt*-thienylvinyl-1,1-dicyanomethylene-3-indanone). [i] ABA-type triblock copolymers comprising A: poly(dimethylsiloxane) and B: poly(diketopyrrolopyrrole-*alt*-diketopyrrolopyrrole).

inferior performance relative to **PNDI2T**, the latter showed a gradual yet consistent decline in mobility over repeated strain cycles, indicating limited mechanical resilience. In contrast to previously reported n-type polymers, the CBS-integrated polymers, particularly ***r*TCDs**, exhibit significantly improved mobility retention and reduced strain sensitivity. To better position our findings within the current research, Table 2 compares recent developments in stretchable n-type semiconductors.[25,26,32,49–51] Among these, polymer **P3** exhibits a similar trend to ***r*TCDs** in achieving directional μ_e uniformity at 60% strain and features a higher initial μ_e.[50] However, its charge transport performance deteriorates substantially upon repeated cycling, with a pronounced decrease in mobility along the parallel direction compared to a single-cycle measurement at the same strain. This instability reflects poor structural resilience under long-term deformation. **ISB**, in contrast, demonstrates excellent mobility isotropy at 60% strain, maintaining balanced transport in both directions during initial straining.[25] However, under repeated stretch–release cycling, **ISB** exhibits anisotropic μ_e retention. This uneven evolution implies an internal reorganization or chain relaxation mechanism that disrupts consistent charge pathways. While the polymer initially performs well under strain, the divergent retention behavior raises concerns about its structural reliability and uniformity of charge transport over prolonged use. Additionally, **ISB's** relatively low μ_e in the unstrained state suggests limited π–π stacking or insufficient molecular order before strain alignment. In contrast, ***r*TCDs** not only retain high intrinsic mobility and directional isotropy at 60% strain but also maintain consistent performance after multiple stretch–release cycles. These results highlight the effectiveness of incorporating DCPD-derived units into CBS design. When properly tuned, the resulting structural complexity enables an optimal balance between mechanical flexibility and microstructural order, providing a promising moiety for developing intrinsically stretchable semiconducting polymers with stable and isotropic charge transport characteristics.

4. Conclusion

In this study, three distinct alicyclic CBSs, a symmetric tricyclic unit (**TCD**), a tricyclic isomeric mixture (***r*TCDs**), and a flexible monocyclic unit (***t*CH**)—were strategically integrated into n-type semiconducting polymers. The investigation reveals that the rigidity and complexity of the CBS structures play a crucial role in determining the polymers' crystallinity, chain orientation, aggregation behaviour, and mobility–stretchability performance under strains. Optical and thermal analyses reveal that the bulky tricyclic structures in **TCD** and ***r*TCDs** promote stronger short-range aggregation than the monocyclic ***t*CH**, as reflected by aggregation fractions of 39%, 37%, and 32%, respectively. This enhanced aggregation corresponds to higher initial μ_es of 0.080 and 0.058 $cm^2\ V^{-1}\ s^{-1}$ for **TCD** and ***r*TCDs**, compared to 0.029 $cm^2\ V^{-1}\ s^{-1}$ for ***t*CH** in the pristine solid state. In addition, a 1 : 1 mixture of **TCD** and ***r*TCDs** provided a μ_e of 0.065 $cm^2\ V^{-1}\ s^{-1}$, which falls between the values for ***r*TCDs** and **TCD**. This implies that the polymer blends of conjugated polymers with isomeric CBS units can be further investigated for developing stretchable semiconductors. Next, structural characterizations further revealed that **TCD** and ***t*CH** adopt predominant face-on and edge-on orientations, both of which are more susceptible to disruption under mechanical strain. In contrast, ***r*TCDs** exhibit a bimodal orientation, providing dual transport pathways that enable more stable charge conduction during deformation. This structural advantage translates into superior mechanical and electrical resilience. After 1000 cycles under 40% strain, ***r*TCDs** outperformed all other polymers, maintaining ($\mu_e^{\parallel}$, $\mu_e^{\perp}$) values of (0.0021, 0.0118) $cm^2\ V^{-1}\ s^{-1}$, with corresponding μ_e retentions of (77, 104)% relative to their single-cycle performance. In comparison, **TCD**, ***t*CH**, and **PNDI2T** exhibited (0.0003, 0.0084), (0.0001, 0.0010), and (0.0024, 0.0103) $cm^2\ V^{-1}\ s^{-1}$ with retention ratios of (21, 131)%, (3, 19)%, and (35, 42)%, respectively. The superior mechanical resilience and isotropic charge transport behaviour of ***r*TCDs** can be attributed to

their moderate structural disorder, reduced long-range crystallinity, and enhanced short-range aggregation. These features collectively facilitate chain adaptability and preserve electronic performance under high mechanical strain. Overall, this work highlights the promise of incorporating structurally isomeric tricyclic CBSs into NDI-based random terpolymers as a compelling strategy to simultaneously optimize mechanical stability without sacrificing their electrical performance.

Author contributions

Ming-Han Chen: investigation, writing – original draft; Yu-Chun Huang: methodology, data curation; Fu-En Szu: synthesizing the alicyclic precursors for conjugation break spacers; Jung-Yao Chen: resources; Man-kit Leung: designing the alicyclic precursors, supervision; Yan-Cheng Lin: conceptualization, formal analysis; manuscript reviewing & editing. All authors read and approved the final manuscript.

Conflicts of interest

The authors declare that they have no conflict of interest.

Data availability

Supplementary information: NMR characterizations of the monomers and polymers; thermal and mechanical characterizations of the polymers; GIWAXS analysis of the pristine and stretched polymer films; FET transfer and output characteristics of the stretched polymer films. See DOI: **https://doi.org/10.1039/D5LF00196J**.

Data is available on request from the corresponding authors.

Acknowledgements

The authors are grateful for the financial support from the National Science and Technology Council in Taiwan (NSTC 113-2221-E-006-013-MY3) and the Featured Area Research Center Program within the framework of the Higher Education Sprout Project, funded by the Ministry of Education (114L9006). The authors also acknowledge the National Synchrotron Radiation Research Center (NSRRC) of Taiwan for the GIWAXS experiments in BL23A1 (TLS). The authors gratefully acknowledge the use of NMR (NMR005000) and elemental analysis (EA000600) of NSTC 112-2740-M-006-001 belonging to the Core Facility Center of National Cheng Kung University.

References

1 Y. Zheng, S. Zhang, J. B. Tok and Z. Bao, *J. Am. Chem. Soc.*, 2022, **144**, 4699–4715.
2 J. Chen, M. Zhu, M. Shao, W. Shi, J. Yang, J. Kuang, C. Wang, W. Gao, C. Zhu, R. Meng, Z. Yang, Z. Shao, Z. Zhao, Y. Guo and Y. Liu, *Adv. Mater.*, 2024, **36**, e2305987.
3 T. W. Chang, Y. C. Weng, Y. T. Tsai, Y. Jiang, N. Matsuhisa and C. C. Shih, *ACS Appl. Mater. Interfaces*, 2023, **15**, 51507–51517.
4 J. Mun, Y. Ochiai, W. Wang, Y. Zheng, Y. Q. Zheng, H. C. Wu, N. Matsuhisa, T. Higashihara, J. B. Tok, Y. Yun and Z. Bao, *Nat. Commun.*, 2021, **12**, 3572.
5 D. Liu, X. Tian, J. Bai, Y. Wang, Y. Cheng, W. Ning, P. K. L. Chan, K. Wu, J. Sun and S. Zhang, *Adv. Sci.*, 2022, **9**, e2203418.
6 S. Dai, X. Zhang, X. Liu, X. Tian, B. Cui, I. Pang, H. Luo, D. Liu, X. He, X. Chen, J. Zhang, Z. Wang, J. Huang and S. Zhang, *Adv. Mater.*, 2025, **37**, e2413951.
7 Y. Wu, Y. Yuan, D. Sorbelli, C. Cheng, L. Michalek, H. W. Cheng, V. Jindal, S. Zhang, G. LeCroy, E. D. Gomez, S. T. Milner, A. Salleo, G. Galli, J. B. Asbury, M. F. Toney and Z. Bao, *Nat. Commun.*, 2024, **15**, 2170.
8 J. S. Park, G. U. Kim, S. Lee, J. W. Lee, S. Li, J. Y. Lee and B. J. Kim, *Adv. Mater.*, 2022, **34**, e2201623.
9 Z. Zhang and Z. Bao, *Natl. Sci. Rev.*, 2023, **10**, nwac093.
10 Z. Zhang, W. Wang, Y. Jiang, Y. X. Wang, Y. Wu, J. C. Lai, S. Niu, C. Xu, C. C. Shih, C. Wang, H. Yan, L. Galuska, N. Prine, H. C. Wu, D. Zhong, G. Chen, N. Matsuhisa, Y. Zheng, Z. Yu, Y. Wang, R. Dauskardt, X. Gu, J. B. Tok and Z. Bao, *Nature*, 2022, **603**, 624–630.
11 W. Liu, C. Zhang, R. Alessandri, B. T. Diroll, Y. Li, H. Liang, X. Fan, K. Wang, H. Cho, Y. Liu, Y. Dai, Q. Su, N. Li, S. Li, S. Wai, Q. Li, S. Shao, L. Wang, J. Xu, X. Zhang, D. V. Talapin, J. J. de Pablo and S. Wang, *Nat. Mater.*, 2023, **22**, 737–745.
12 Z. Shangguan, C. Li, L. Chen, X. Xue, K. Chenchai, X. Zhang, Y. Li, X. Zhang, G. Zhang and D. Zhang, *Polym. Sci. Technol.*, 2025, **1**, 351–358.
13 R. Chen, Y. Liu, T. Li, Z. Peng, H. Li, S. Huang, Z. Ding, X. Duan, Y.-Q.-Q. Yi and Y. Han, *J. Mater. Chem. C*, 2025, **13**, 10857–10870.
14 K. Liu, B. Ouyang, X. Guo, Y. Guo and Y. Liu, *npj Flexible Electron.*, 2022, **6**, 1.
15 M. H. Kim, M. W. Jeong, J. S. Kim, T. U. Nam, N. T. P. Vo, L. Jin, T. I. Lee and J. Y. Oh, *Sci. Adv.*, 2022, **8**, eade2988.
16 S. Zhang, Y. H. Cheng, L. Galuska, A. Roy, M. Lorenz, B. Chen, S. Luo, Y. T. Li, C. C. Hung, Z. Qian, P. B. J. St. Onge, G. T. Mason, L. Cowen, D. Zhou, S. I. Nazarenko, R. F. Storey, B. C. Schroeder, S. Rondeau-Gagné, Y. C. Chiu and X. Gu, *Adv. Funct. Mater.*, 2020, **30**, 2000663.
17 Y. Wang, K. L. Chen, N. Prine, S. Rondeau-Gagné, Y. C. Chiu and X. Gu, *Adv. Funct. Mater.*, 2023, **33**, 2306576.
18 M. Ashizawa, Y. Zheng, H. Tran and Z. Bao, *Prog. Polym. Sci.*, 2020, **100**, 101181.
19 Y. Ding, Y. Yuan, N. Wu, X. Wang, G. Zhang and L. Qiu, *Macromolecules*, 2021, **54**, 8849–8859.
20 D. Liu, J. Mun, G. Chen, N. J. Schuster, W. Wang, Y. Zheng, S. Nikzad, J. C. Lai, Y. Wu, D. Zhong, Y. Lin, Y. Lei, Y. Chen, S. Gam, J. W. Chung, Y. Yun, J. B. Tok and Z. Bao, *J. Am. Chem. Soc.*, 2021, **143**, 11679–11689.
21 L. Ding, Z. D. Yu, X. Y. Wang, Z. F. Yao, Y. Lu, C. Y. Yang, J. Y. Wang and J. Pei, *Chem. Rev.*, 2023, **123**, 7421–7497.

22 A. X. Chen, A. T. Kleinschmidt, K. Choudhary and D. J. Lipomi, *Chem. Mater.*, 2020, **32**, 7582–7601.
23 Y.-C. Lin, M. Matsuda, C.-K. Chen, W.-C. Yang, C.-C. Chueh, T. Higashihara and W.-C. Chen, *Macromolecules*, 2021, **54**, 7388–7399.
24 M. Matsuda, C.-Y. Lin, K. Enomoto, Y.-C. Lin, W.-C. Chen and T. Higashihara, *Macromolecules*, 2023, **56**, 2348–2361.
25 M. Matsuda, C. Y. Lin, C. Y. Sung, Y. C. Lin, W. C. Chen and T. Higashihara, *ACS Appl. Mater. Interfaces*, 2023, **15**, 51492–51506.
26 F. Zhang, J. Sun, F. Liu, J. Li, B. L. Hu, Q. Tang and R. W. Li, *ACS Appl. Mater. Interfaces*, 2024, **16**, 38324–38333.
27 C. An, W. Dong, D. Pei, X. Qin, Z. Wang, B. Zhao, L. Bu, H. Chen, Y. Han, C. Chi and Y. Geng, *Macromolecules*, 2023, **56**, 5314–5325.
28 J. Y. Oh, S. Rondeau-Gagne, Y. C. Chiu, A. Chortos, F. Lissel, G. N. Wang, B. C. Schroeder, T. Kurosawa, J. Lopez, T. Katsumata, J. Xu, C. Zhu, X. Gu, W. G. Bae, Y. Kim, L. Jin, J. W. Chung, J. B. Tok and Z. Bao, *Nature*, 2016, **539**, 411–415.
29 A. Kim, Y. Ahn, W. Li, S. H. Park, M. J. Cho, D. H. Choi and H. Yang, *ACS Appl. Mater. Interfaces*, 2023, **15**, 58663–58672.
30 M. Zhu, Y. Li, C. Wang, Z. Shao, W. Shi, J. Chen, Z. Yang, Y. Bian, M. Qin, Z. Zhu, Z. Zhao, H. Wang, Y. Guo and Y. Liu, *Chem. Mater.*, 2024, **36**, 8274–8285.
31 J. Mun, G. J. N. Wang, J. Y. Oh, T. Katsumata, F. L. Lee, J. Kang, H. C. Wu, F. Lissel, S. Rondeau-Gagné, J. B. H. Tok and Z. Bao, *Adv. Funct. Mater.*, 2018, **28**, 1804222.
32 X. Yu, L. Chen, C. Li, C. Gao, X. Xue, X. Zhang, G. Zhang and D. Zhang, *Adv. Mater.*, 2023, **35**, e2209896.
33 N. Asim, M. Badiei, M. Torkashvand, M. Mohammad, M. A. Alghoul, S. S. Gasaymeh and K. Sopian, *J. Cleaner Prod.*, 2021, **67**, 1259–1266.
34 S. Fuchs, M. Steffen, A. Dobrowolski, T. Rösler, L. Johnen, G. Meier, H. Strutz, A. Behr and A. J. Vorholt, *Catal. Sci. Technol.*, 2017, **7**, 5120–5127.
35 S. Fuchs, D. Lichte, T. Jolmes, T. Rösler, G. Meier, H. Strutz, A. Behr and A. J. Vorholt, *ChemCatChem*, 2018, **10**, 4126–4133.
36 C. M. Lin, C. H. Chen, C. H. Lin, W. C. Su and T. Y. Juang, *ACS Omega*, 2018, **3**, 4295–4305.
37 M.-C. Mi, F.-E. Szu, Y.-C. Cheng, C.-H. Tsai, J.-H. Chen, J.-H. Huang, C.-C. Kuo, Y.-C. Lin, M.-K. Leung and W.-C. Chen, *ACS Appl. Polym. Mater.*, 2024, **6**, 11137–11148.
38 X. Guo and M. D. Watson, *Org. Lett.*, 2008, **10**, 5333–5336.
39 F.-E. Szu, C.-W. Yang, Y.-Z. Li, Y.-Y. Yu, C.-I. Huang, J.-H. Chen, J.-H. Huang and M.-K. Leung, *J. CO2 Util.*, 2025, **100**, 103177.
40 Y.-C. Lin, K. Terayama, K. Yoshida, P.-J. Yu, P.-H. Chueh, C.-C. Chueh, T. Higashihara and W.-C. Chen, *Mater. Chem. Front.*, 2022, **6**, 891–900.
41 J. S. Chickos, D. Hillesheim, G. Nichols and M. J. Zehe, *J. Chem. Thermodyn.*, 2002, **34**, 1647–1658.
42 D. Rijal, V. Vasilyev, Y. Yang and F. Wang, *Processes*, 2025, **13**, 543.
43 R. Matsidik, H. Komber, A. Luzio, M. Caironi and M. Sommer, *J. Am. Chem. Soc.*, 2015, **137**, 6705–6711.
44 S. Park, M. H. Lee, K. S. Ahn, H. H. Choi, J. Shin, J. Xu, J. Mei, K. Cho, Z. Bao, D. R. Lee, M. S. Kang and D. H. Kim, *Adv. Funct. Mater.*, 2016, **26**, 4627–4634.
45 X. Liu, T. Jin, H. Li, S. Wang, Z. Shen, J. Li, R. Chen, Y. Chen and Y. Han, *Macromolecules*, 2024, **57**, 4141–4157.
46 R. Song, H. Schrickx, N. Balar, S. Siddika, N. Sheikh and B. T. O'Connor, *Macromolecules*, 2020, **53**, 1988–1997.
47 N. Balar, J. J. Rech, S. Siddika, R. Song, H. M. Schrickx, N. Sheikh, L. Ye, A. Megret Bonilla, O. Awartani, H. Ade, W. You and B. T. O'Connor, *Adv. Funct. Mater.*, 2021, **32**, 2105597.
48 H.-C. Wu, S. Nikzad, C. Zhu, H. Yan, Y. Li, W. Niu, J. R. Matthews, J. Xu, N. Matsuhisa, P. K. Arunachala, R. Rastak, C. Linder, Y.-Q. Zheng, M. F. Toney, M. He and Z. Bao, *Nat. Commun.*, 2023, **14**, 8382.
49 S. Yamamoto, M. Matsuda, C.-Y. Lin, K. Enomoto, Y.-C. Lin, W.-C. Chen and T. Higashihara, *ACS Appl. Polym. Mater.*, 2022, **4**, 8942–8951.
50 C. H. Chung, Y. C. Huang, S. W. Su, C. J. Su, U. S. Jeng, J. Y. Chen and Y. C. Lin, *Macromol. Rapid Commun.*, 2025, **46**, e2401057.
51 Y. Cho, J. Park, S. Jeong, H. Park, H. W. Kim, J. H. Oh and C. Yang, *Chem. Mater.*, 2022, **34**, 1554–1566.